THE JOURNAL OF PHYSICAL CHEMISTRY B

Article

pubs.acs.org/JPCB

Characterizing the Structure of Organic Molecules of Intrinsic Microporosity by Molecular Simulations and X-ray Scattering

Lauren J. Abbott,[†] Amanda G. McDermott,[†] Annalaura Del Regno,[‡] Rupert G. D. Taylor,[§] C. Grazia Bezzu,[§] Kadhum J. Msayib,[§] Neil B. McKeown,[§] Flor R. Siperstein,[‡] James Runt,[†] and Coray M. Colina*,[†]

[†]Department of Materials Science and Engineering, The Pennsylvania State University, University Park, Pennsylvania 16802, United States

[‡]School of Chemical Engineering and Analytical Science, The University of Manchester, Manchester M13 9PL, United Kingdom

[§]School of Chemistry, Cardiff University, Cardiff CF10 3AT, United Kingdom

Supporting Information

ABSTRACT: The design of a new class of materials, called organic molecules of intrinsic microporosity (OMIMs), incorporates awkward, concave shapes to prevent efficient packing of molecules, resulting in microporosity. This work presents predictive molecular simulations and experimental wide-angle X-ray scattering (WAXS) for a series of biphenyl-core OMIMs with varying end-group geometries. Development of the utilized simulation protocol was based on comparison of several simulation methods to WAXS patterns. In addition, examination of the simulated structures has facilitated the assignment of WAXS features to specific intra- and intermolecular distances, making this a useful tool for characterizing the packing behavior of this class of materials. Analysis of the simulations suggested that OMIMs had greater microporosity when the molecules were the most shape-persistent, which required rigid structures and bulky end groups. The simulation protocol presented here allows for predictive, presynthesis screening of OMIMs and similar complex molecules to enhance understanding of their structures and aid in future design efforts.

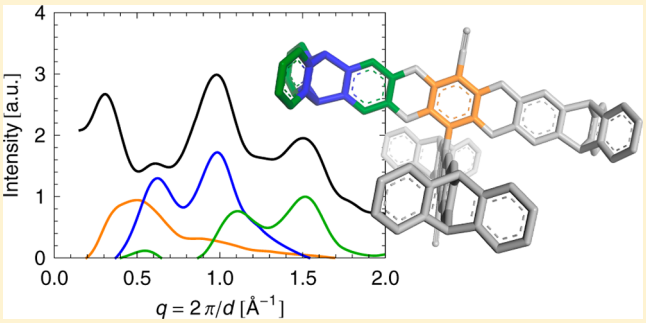

1. INTRODUCTION

Microporous materials have pores on the order of molecular dimensions (smaller than 2 nm), which are of interest for applications like gas storage, separations, and catalysis. These materials are often networks, since the rigidity of the networked systems enables pore formation by preventing a more favorable, dense packing. A wide range of networks have been explored, including crystalline materials like zeolites[1] or metal−organic frameworks (porous coordination polymers),[2,3] as well as amorphous materials such as activated carbons[4] or hyper-crosslinked polymers.[5] More recently, linear polymers of intrinsic microporosity (PIMs)[6] have been introduced as an alternative to networks, most importantly because they are solution-processable. PIMs induce porosity intrinsically through the inclusion of rigid and contorted structures that promote inefficient packing. Other efforts have begun to focus on discrete molecules, which interact by noncovalent interactions only. Microporosity in discrete molecules has been achieved by both crystalline and amorphous structures containing extrinsic and/or intrinsic microporosity. Molecular crystals can exhibit extrinsic porosity, for example, through formation of a framework of cooperative hydrogen bonding.[7] Alternatively, a number of cage compounds consisting of intrinsic (and extrinsic) microporosity have been reported, which can exist in either crystalline or amorphous states.[8−11] Lastly, a number of iptycene-based materials presented in the literature induce intrinsic microporosity through molecular units with void spaces and clefts that provide "internal molecular free volume."[12−14]

Organic molecules of intrinsic microporosity (OMIMs) are a class of discrete molecules of rigid and awkward shapes, using similar chemistries as PIMs, that achieve porosity through inefficient packing.[6,15] The fundamental motivation for the design of OMIMs can be linked to mathematical studies of geometric shapes. Using a random jamming modeling technique, Jiao et al. found that the maximum packing density of concave two-dimensional superdisks[16] and three-dimensional superballs[17] decreased with increasingly concave faces. The molecular building blocks of OMIMs, therefore, were designed to mimic concave geometries. A series of OMIMs were recently synthesized[15] containing a biphenyl core (**5**) of cruciform shape and terminal units of various geometries: trigonal (**1**),

Received: September 4, 2012
Revised: November 9, 2012
Published: December 5, 2012

tetrahedral (**2**), and octahedral (**3**), which gave OMIM-1 (**1**+**5**), OMIM-2 (**2**+**5**), and OMIM-3 (**3**+**5**), respectively. A functionalized version of terminus 1 (**4**) was also studied, which produced OMIM-4 (**4**+**5**). The structures of precursors **1**−**5** and OMIMs 1−4 are shown in Figure 1. These OMIMs were determined to be microporous by nitrogen adsorption and apparent BET surface areas in the range 477−626 m^2 g^{-1}.[15]

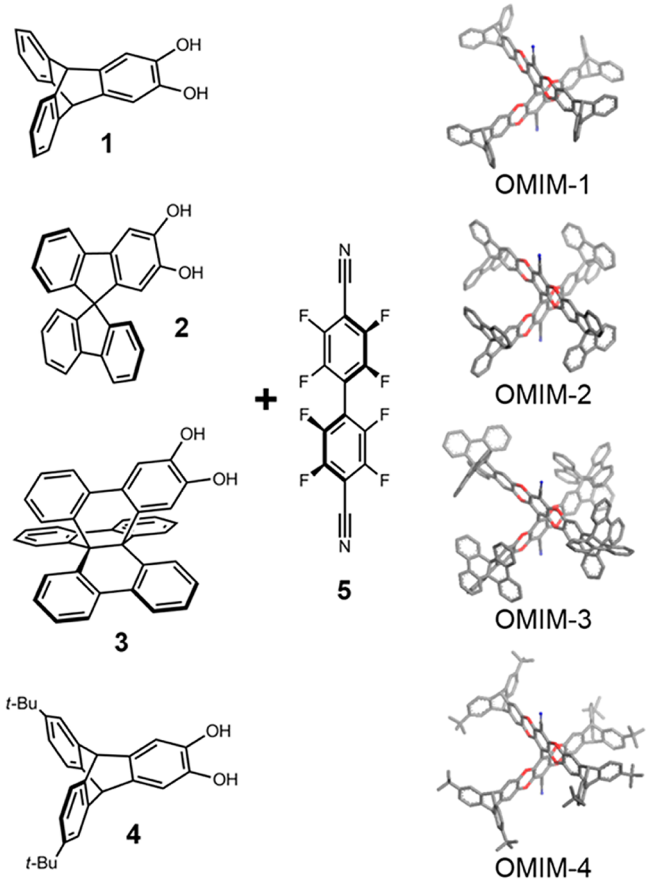

Figure 1. Chemical structures of terminal (**1**−**4**) and core (**5**) precursors and the resulting biphenyl-core OMIMs. Pairing of the core and one terminus results in OMIM-1 (**1**+**5**), OMIM-2 (**2**+**5**), OMIM-3 (**3**+**5**), and OMIM-4 (**4**+**5**). Note that hydrogen atoms are not shown in the OMIM models for clarity.

Although these OMIMs are discrete molecules, they are of moderate sizes with molecular masses greater than 1300 g mol^{-1}. The synthesis of these molecules is complicated by their large sizes, as well as the inherent steric hindrances associated with the awkward shapes. Therefore, molecular simulations can be beneficial in two ways: (a) providing a screening process of OMIMs not yet synthesized and (b) enhancing understanding of the structures and packing behavior of OMIMs. The large and complex nature of amorphous OMIMs, however, also complicates the generation of consistent and realistic molecular models. In order to utilize simulations in a predictive capacity, the development of a methodology sufficient for accurate, predictive models was essential.

This work presents a general procedure for simulation of OMIMs, or other complex molecules, that is predictive knowing only the chemical structure, as well as initial insight into their structures and packing behavior. In section 2, the simulation and experimental methodology are provided. Development of the predictive simulation protocol was carried out by comparison of several simulation procedures with experimental wide-angle X-ray scattering (WAXS) data, which is discussed in section 3.1. The presented simulation approach is then further validated against the series of biphenyl-core OMIMs (Figure 1), given in section 3.2. In section 3.3, interpretation of the WAXS data is provided by analysis of the simulation models to determine characteristic components within the system associated with the WAXS features. The effect of the end-group geometries and molecular rigidity on the packing behavior and resulting structures is assessed in section 3.4. Lastly, some additional discussion of the simulation methods is provided in section 3.5, before concluding remarks in section 4.

2. METHODS

2.1. Simulation Structure Generation. Molecular simulations of amorphous materials require a methodology to consistently generate simulation models that accurately reflect experimental samples. This work considers several approaches to structure generation of OMIMs to determine the one most consistent with available experimental data. Particular interest has been placed here on the development of a methodology that provides predictive simulations, knowing only the chemical structure of the molecules, as a means for screening of molecules not yet synthesized. Descriptions of the approaches taken in this work are described below as methods 1−4.

Method 1. A united-atom model was used to describe the molecules with Lennard-Jones parameters derived from the TraPPE force field,[18] which has been effective in simulations of polymers of similar chemistry;[19] charges were omitted in these simulations. Molecular conformations of a single molecule were sampled from an NVT molecular dynamics (MD) simulation at 600 K in LAMMPS.[20] These initial conformations were randomly selected and packed into a periodic simulation box at a specified final density. Insertions of molecules were made at random, avoiding only hard-core overlaps ($r_{overlap}$ = 1.0 Å). Once packed, the box underwent a Monte Carlo (MC) simulated annealing procedure performed with an in-house code, during which the system was cooled from 4000 to 20.6 K.

Method 2. Fully atomistic models were employed with interactions described by the polymer consistent force field (PCFF) and charges assigned by a bond-increment approach.[21] Molecules were packed into the periodic box to a specified final density based on an MC packing procedure, where higher weight was given to insertions of molecules associated with lower energies. After packing, a four-step NVT MD protocol (Table S1 of the Supporting Information) was applied to fully relax the system. All simulations were carried out using Materials Studio 5.5.[22]

Method 3. Fully atomistic models were described using the OPLS force field[23] with charges omitted. Molecules were packed randomly into a low density box, avoiding overlaps of the van der Waals radii. The box was then scaled incrementally to a specified final density. Once at the final density, an MD protocol consisting of seven NVT and NPT steps (Table S2 of the Supporting Information) was performed. Then, the box was scaled back to the specified final density and a final NVT simulation at 300 K was performed. All simulations were performed in Gromacs 4.[24]

Method 4. This method was a modification to method 2 to allow for predictive simulations of systems with an unknown final density. Unlike method 2, molecules were packed into the

dx.doi.org/10.1021/jp308798u | J. Phys. Chem. B 2013, 117, 355−364

periodic simulation box at a low initial density using the MC packing procedure. Then a 21-step NVT/NPT MD compression protocol[19] (Table S3 of the Supporting Information) was performed. It is important to stress that the final density was not predetermined, but obtained intrinsically from the compression scheme, allowing for predictive simulations. This 21-step compression has been used to achieve accurate and consistent system densities in simulations of hypercrosslinked polymers[25] and PIMs.[19] (Further simulation details for all methods are provided in the Supporting Information.)

2.2. Simulation Characterization. Molecular models were characterized in this work by densities, surface areas, pore volumes, and structure factors. All results were averaged over five independent simulation boxes for each system. Total and skeletal densities were calculated from the total simulation volume and skeletal volume, respectively. The porosity in the simulations was measured geometrically by surface areas and pore volumes. By this approach, surfaces can be thought of as being defined by rolling a probe molecule across the surface of atoms. A probe size equal to the kinetic diameter of a nitrogen molecule (d_{N2} = 3.681 Å) was used,[26] as experimental BET surface areas were determined from nitrogen isotherms.

Structure factors of the molecular models, which can be compared to experimental X-ray scattering data, were computed using ISAACS v2.2[27] from a Fourier transform of the sum of partial radial distribution functions $g_{AB}(r)$, which represents the probability of finding an atom of species B at a distance r from an atom of species A, normalized to 1 at large distances (Equation S1 in the Supporting Information). Partial structure factors were also obtained using a scaled Faber–Ziman definition (Equation S2 in the Supporting Information).[28] Defined in this way, the scaled partial structure factors give the exact contribution to the total structure factors, i.e., $S(q) = \sum_{A,B} S_{AB}(q)$. (Further simulation details of characterization methods are provided in the Supporting Information.)

2.3. X-ray Scattering. Powder OMIMs were precipitated from solution in solvent by the addition of methanol; prior to scattering measurements, they were degassed in a vacuum oven at 120–130 °C for 24 h or longer. Although methanol treatment of PIMs immediately prior to measurements increased film permeability via the removal of adsorbed species[29] and also influenced PIM scattering patterns,[28] soaking OMIMs in methanol just before degassing had a negligible effect on amorphous powder scattering patterns. The data shown is from untreated powders.

WAXS patterns were collected at room temperature with a Rigaku DMAX-RAPID instrument using an image-plate detector and Cu Kα radiation (λ = 1.54 Å). Isotropic two-dimensional patterns were azimuthally averaged into one-dimensional profiles of intensity $I(q)$ vs scattering vector $q = 4\pi \sin(\theta)/\lambda$, and backgrounds from Kapton windows were subtracted from all scattering patterns. Due to the particulate nature of the powder samples, low-q power-law scattering was observed, overlapping significantly with the lowest-q peak at 0.34–0.38 Å^{-1}. To improve comparison with $S(q)$ from nonparticulate simulated materials, the particulate power-law contribution was fit to small-angle X-ray scattering (SAXS) data from 0.02 to 0.17 Å^{-1} and subtracted from the WAXS patterns (Figure S1 in the Supporting Information). SAXS patterns were collected using a Molecular Metrology instrument with a pinhole camera, multiwire area detector, and sample-to-detector distance of 0.5 m.

3. RESULTS AND DISCUSSION

3.1. Analysis of Simulation Methods. Molecular models of OMIMs were generated using four different simulation methodologies to determine an appropriate approach for generating simulation models consistent with experimental samples. All procedures were applied first to OMIM-1 (Figure 1) for comparison by structural and porosity measurements. Methods 1–3 are fixed-density techniques, meaning that the final density of the system was predefined. The final density has a large effect on the properties of the material, so models were generated with methods 1–3 at a range of densities (0.7, 0.85, and 1.0 g cm^{-3}) in order to determine those closest in agreement to structural experimental data. Method 4 was introduced as a parameter-free technique to allow for predictive simulations; i.e., the final density was not fixed using this approach. This method is desirable for providing predictive simulations of molecules not yet synthesized.

The average calculated properties for five independent boxes at each density using methods 1–3 are given in Table 1. In examining the properties of OMIM-1 for each data set, it is clear that both the density and simulation method significantly impact the final structure obtained. For each simulation method, the average accessible surface area decreased substantially with increasing density, as shown in Figure 2. Additionally, at a given density, the surface areas varied widely from one method to another. Average surface areas at a density of 1.0 g cm^{-3}, for example, ranged from 192 to 730 m^2 g^{-1}. However, the relative magnitudes of surface areas obtained with the different methods were constant at each density: method 1 always yielded the largest surface area and method 3 the smallest.

Table 1. Properties of Simulated OMIM-1 at Various Densities Using Four Different Simulation Methods[a]

method	no. of molecules	total density (g cm^{-3})	surface area (m^2 g^{-1})
1	68	0.704	2053 (15)
	83	0.851	1212 (41)
	98	1.005	730 (24)
2	69	0.700	1905 (45)
	83	0.850	976 (25)
	100	1.000	315 (18)
3	68	0.697	1588 (41)
	83	0.851	645 (25)
	98	1.005	192 (11)
4	100	1.085(8)	155 (21)

[a]Results were averaged over five independent boxes for each method at each density. Values are reported as the mean and standard deviations are given in parentheses if not 0.

The deviation between the methods may be partially attributed to the proximity of the simulated samples to mechanical equilibrium. Since method 1 incorporated only MC translation and rotation steps, molecules were constrained to rigid conformations. The equilibration of this method was therefore limited, as the molecules could not change configurations to increase attractive intra- and intermolecular interactions. The MD techniques (methods 2 and 3), on the other hand, more adequately equilibrated the system. The molecular flexibility provided for more efficient packing of the molecules, as they were able to bend and contort to fill free space. The more efficient packing of the MD techniques

dx.doi.org/10.1021/jp308798u | J. Phys. Chem. B 2013, 117, 355–364

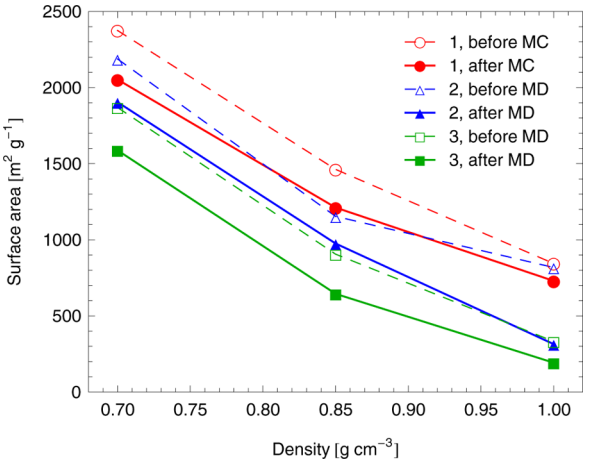

Figure 2. Accessible surface area versus total density of OMIM-1 molecular models generated using methods 1−3. Surface areas are given as calculated before (dashed lines, open symbols) and after (solid lines, filled symbols) MC or MD equilibration steps. Results were averaged over five independent boxes for each set. Standard deviations are not shown for clarity, but are given in Table 1.

resulted in lower porosity, as shown by the accessible surface areas in Table 1.

The effects of the MC simulated annealing and MD relaxations were examined more closely by comparing the surface areas of each box before and after the MC/MD steps were performed, as shown in Figure 2. For each method at each density, the surface areas decreased after the MC/MD steps, consistent with an equilibration of the structures. The inadequacy of the MC simulated annealing (method 1) in comparison to the MD methods (methods 2 and 3) was exaggerated at the highest density, 1.0 g cm^{-3}. The decrease in surface area at this density after the MC simulated annealing (method 1) was only about 13%, compared to the MD relaxation of method 2, which resulted in a drop of approximately 61%. The poor equilibration of the MC method was quantified additionally by the average atomic displacements measured during the simulated annealing, which were 5.5, 3.0, and 1.9 Å at densities 0.7, 0.85, and 1.0 g cm^{-3}, respectively (Supporting Information Figure S2). The limited displacement of the molecules at higher densities during the MC simulated annealing suggests the rigid molecules were trapped in a frustrated packing state and unable to adequately rearrange to reach a denser, more relaxed configuration.

In comparison, the average surface areas of method 2 before MD steps were smaller than those of method 1 before MC steps at each density. This is most likely a result of the initial packing procedures used in each method. The initial packing in method 1 was performed randomly, only avoiding hard core overlaps. Method 2, on the other hand, employed an MC packing scheme, such that molecule insertions associated with lower energies were made more favorably. It is important to note that the MC packing scheme of method 2 is different than the MC simulated annealing used in method 1 after the initial random packing. Since method 2 employed an MC packing scheme, the packed boxes can be considered most similar to method 1's boxes after the MC simulated annealing was performed. As can be seen in Figure 2, the surface areas of the annealed boxes of method 1 and the packed boxes of method 2 are very similar at all densities. The further drop in surface area after the MD protocol for method 2 was the result of the more thorough equilibration achieved by the MD procedure, which incorporated molecular flexibility. This difference was exaggerated at the highest density, 1.0 g cm^{-3}, where the MC procedure was restricted due to the rigid-molecule constraints. Method 3 resulted in even lower average surface areas before MD steps than method 2. This may be a consequence of the scaling procedure used to produce the initial packed box.

Additional assessment and validation of the simulation methods was provided by comparison of the simulated structure factors to experimental WAXS data, which are plotted in Figure 3. The WAXS pattern for OMIM-1 has three features of interest in the low q range (<2 Å^{-1}): peak A at 0.376 Å^{-1} (16.7 Å), peak B at 0.95 Å^{-1} (6.6 Å), and peak C at 1.33 Å^{-1}

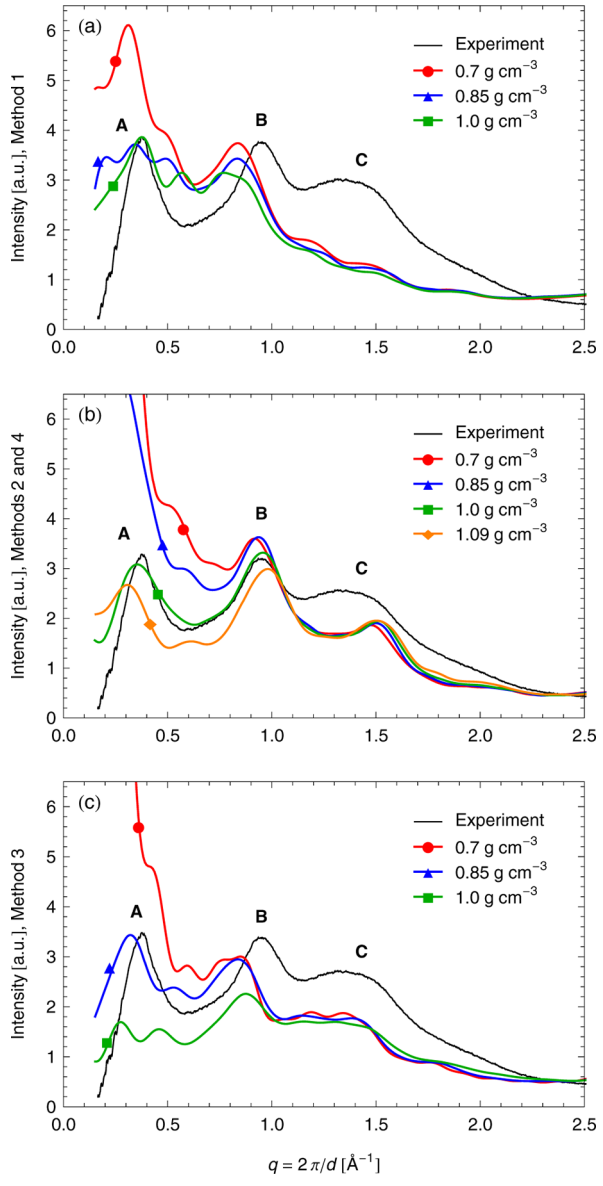

Figure 3. Wide-angle X-ray scattering (WAXS) data compared to average simulated structure factors of OMIM-1 at densities 0.7, 0.85, and 1.0 g cm^{-3} using (a) methods 1, (b) 2, and (c) 3. The average structure factor for method 4, with a density of 1.085 g cm^{-3}, is also shown with method 2 in (b). The three characteristic WAXS features are labeled A, B, and C. For all simulations, the structure factors are given as an average over five independent simulations. The relative scaling of experimental and simulated data is arbitrary.

dx.doi.org/10.1021/jp308798u | J. Phys. Chem. B 2013, 117, 355−364

(4.7 Å), each labeled in Figure 3. As was observed for the surface areas, significant variability was also seen in the simulated structure factors. Variation among the structure factors at different densities was expected, since the density has a direct impact on the structure of the system. However, the patterns from the three methods also varied considerably in the number of peaks, peak positions, and relative peak intensities, suggesting fundamental differences in their structures. Method 2 showed the best agreement with the peak positions and relative intensities of peaks A and B. Methods 1 and 3, on the other hand, resulted in a position of peak B at lower q values, as well as an extra small feature between A and B. A significant difference was observed in peak C among the structure factors obtained from methods 1−3. This feature was present in both MD procedures (methods 2 and 3) but varied in position and breadth. With method 1, peak C was not reproduced at all. Overall, the molecular models most consistent with the WAXS data were those obtained using method 2 at a density of 1.0 g cm^{-3}.

The results reported for methods 1−3 illustrate the importance of the simulation densities for the accuracy of the molecular models. Predictive molecular simulations require a methodology that produces consistent, accurate results with as few input parameters as possible. This is particularly important since densities can be difficult to determine experimentally and depend heavily on the method being used. Since methods 1−3 each required a final density to be specified, method 4 was introduced. Unlike the other techniques, method 4 did not require knowledge of a final density, since instead the density was determined implicitly by the MD compression scheme employed. Therefore, with method 4, simulations of OMIMs can be performed in a predictive capacity without prior knowledge of the density. This is important especially for systems as large and complex as OMIMs.

Along with the results for methods 1−3, the average properties for the molecular models obtained with method 4 are given in Table 1, and the average structure factor is shown in Figure 3 with those for method 2. The average density obtained using method 4 was 1.085 g cm^{-3}, which is higher than the 1.0 g cm^{-3} density examined with methods 1−3. Consistent with the higher density, the average accessible surface area was smaller than that of method 2 at 1.0 g cm^{-3}. Despite the lower porosity, the average $S(q)$ compared well to that of method 2 at density 1.0 g cm^{-3} and WAXS data, showing the same overall shape with only slight shifts in the positions of peaks A and B. However, method 4 offered results consistent with experimental data with the additional benefit of not requiring prior knowledge of any experimental data, including density, thus allowing for predictive simulations. Method 4, therefore, is proposed here as the best procedure for simulating OMIMs of unknown density.

3.2. Characterization of Biphenyl-Core OMIMs. By varying the molecular geometry of the OMIMs, it is possible to adjust the molecular packing to fine-tune the porosity. To study the effect of the end-group geometry on packing behavior, simulations were performed using method 4 on the series of biphenyl-core OMIMs in Figure 1. These OMIMs have increasingly bulky end groups designed to provide greater molecular concavities and more effectively inhibit efficient packing. OMIMs 2−4 have several possible regioisomers depending on the orientation of the end groups in relation to the core; experimental samples are likely derived from a mixture of these regioisomers. However, to simplify the structures for the simulations, only pure compositions were considered. Two different regioisomers of OMIM-2, 2a and 2b (Figure S3 of the Supporting Information), were examined, which were chosen to represent extreme cases of the molecular shapes most dissimilar. Only one regioisomer each of OMIMs 3 and 4 was simulated, however, because others were not expected to be significantly different.

Simulated characterization of five independent samples of each biphenyl-core OMIM resulted in the average properties given in Table 2. Experimental BET surface areas (477−626 m^2 g^{-1}) were significantly higher than the geometric surface areas from the simulations measured here (88−286 m^2 g^{-1}) but were in better agreement with BET surface areas calculated from simulated nitrogen adsorption isotherms (416−568 m^2 g^{-1}), which is discussed in more detail elsewhere.[15] An interesting observation from the simulations was that the porosity did not increase with end-group bulkiness. OMIM-2, for example, which has a bulkier end group than OMIM-1, had a smaller surface area and pore volume. Similarly, OMIM-3, which has the bulkiest end group, resulted in less porosity than OMIM-4. On the contrary, OMIM-4, which added *tert*-butyl groups on the triptycene end groups of OMIM-1, successfully increased the porosity. By comparison of the geometrical shapes of the four end groups and their resulting porosities, it appears that, to increase the porosity of the OMIMs, awkward end groups must increase the concavity of the structure without increasing its bulkiness to the point where pore filling may occur. These OMIMs demonstrate the delicate balance between these two factors, which will be discussed in more detail below.

Table 2. Properties of Simulated Biphenyl-Core OMIMs[a]

OMIM	total density (g cm^{-3})	skeletal density (g cm^{-3})	pore volume (cm^3 g^{-1})	surface area (m^2 g^{-1})
1	1.085(8)	1.310(3)	0.158(8)	155 (21)
2a	1.114(8)	1.304(4)	0.131(8)	92 (19)
2b	1.12(1)	1.300(3)	0.125(7)	88 (9)
3	1.074(8)	1.339(5)	0.184(9)	194 (26)
4	0.923(9)	1.191(2)	0.24(1)	286 (21)

[a]Results were averaged over five independent boxes for each system. Values are reported as the mean and standard deviations are given in parentheses.

Further characterization of the OMIM simulations was provided by structure factors, which show excellent agreement with experimental WAXS data, as shown in Figure 4. Like OMIM-1, the WAXS patterns for OMIMs 2−4 have three characteristic features, labeled A, B, and C in Figure 4, the positions of which are listed in Table S4 of the Supporting Information. While the positions of peak B in the simulations were similar to the WAXS data in all cases, more variability existed in peak A (illustrated by the error bars in Figure S4 of the Supporting Information). Additionally, the position and breadth of peak C was not captured properly among the four OMIMs. Other slight discrepancies exist in the simulations, such as small features or shoulders not present in the experimental data. One possible source of discrepancies could be the use of force field generated charges instead of ab initio charges in the simulations. Ab initio charges are calculated for the specific molecule of interest, so they more accurately reflect the electronic nature of the material. Another source could be regioisomers. The simulations only considered pure compositions of OMIMs 2−4, which contain mixtures of regioisomers

dx.doi.org/10.1021/jp308798u | J. Phys. Chem. B 2013, 117, 355−364

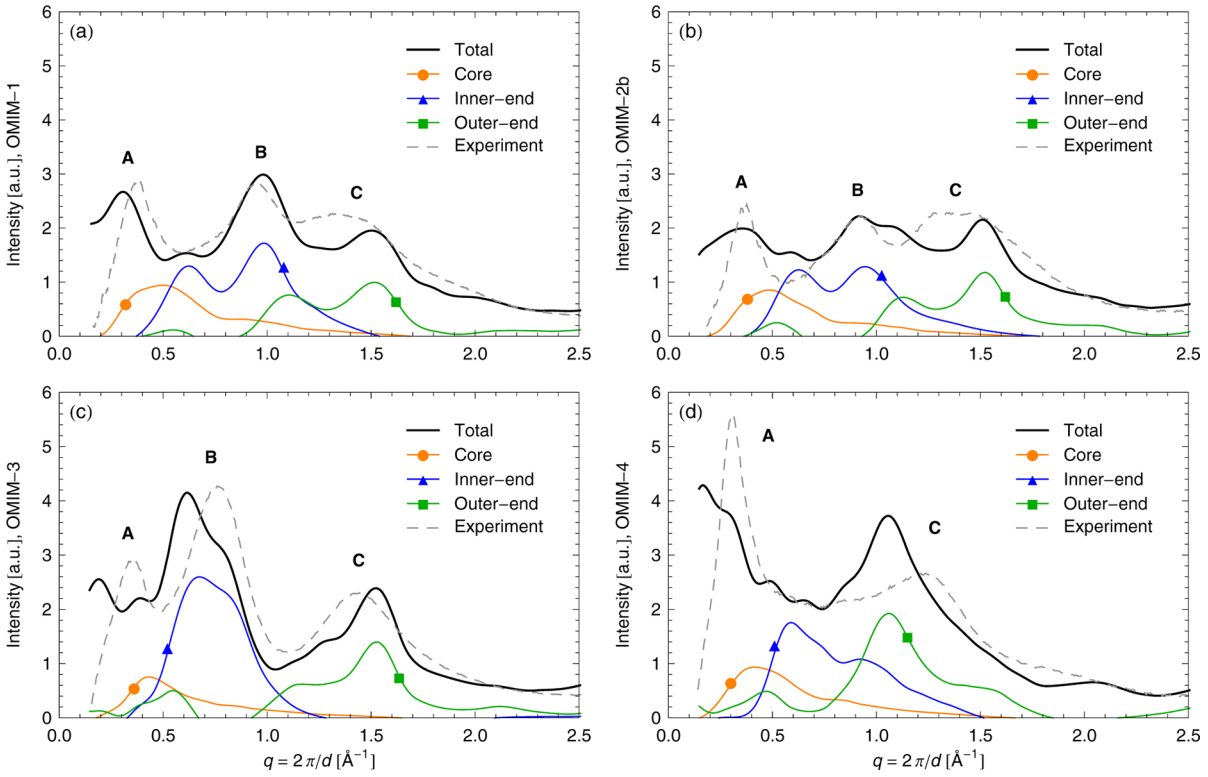

Figure 4. Wide-angle X-ray scattering (WAXS) data (dashed lines) and simulated structure factors (solid lines) of (a) OMIM-1, (b) OMIM-2b, (c) OMIM-3, and (d) OMIM-4. The partial structure factors (solid lines and closed symbols) correspond to the atom groups that are defined in Figure 5. The three characteristic WAXS features are labeled A, B, and C. For all simulations, the structure factors are given as an average over five independent simulations; error bars for the structure factors are shown in Figure S4 of the Supporting Information. The relative scaling of experimental and simulated data is arbitrary.

in experimental samples. Better agreement with WAXS data could be achieved by considering either of these factors; however, this was outside the scope of the present work. Although some inconsistencies were present in the simulated structure factors, the overall agreement with WAXS data was excellent considering the predictive nature of the methodology (method 4).

3.3. Interpretation of Scattering. In order to interpret the scattering patterns, a deeper understanding of the structure was required. The molecular simulations contributed significantly in this regard, since the models provided necessary atomistic detail to enable the determination of characteristic distances within the structures. In particular, the structure factors were broken down into partial contributions to assign scattering features to key components of each system, as was done for PIM-1 in previous work.[28] Each biphenyl-core OMIM was divided into three groups of interest, which are color-coded along one of the arms of the molecular models of OMIMs 1−4 in Figure 5: core atoms (orange), inner end-group atoms (blue), and outer end-group atoms (green). The self-contribution partial structure factors for these groupings (i.e., $S_{core-core}$, $S_{inner-inner}$, and $S_{outer-outer}$) are given along with the total structure factors in Figure 4 in colors corresponding to their atom groups. The partial structure factors were utilized to interpret the scattering features in order to improve understanding of the packing behavior of OMIMs.

From the partial structure factors in Figure 4, the characteristic separation distances of the atom groups were identified and associated with the scattering features. These contributions to the three characteristic scattering features were found to be similar among each of the biphenyl-core OMIMs. Peak C was observed to be related to the outer end-group atoms (green), while the inner end-group atoms or end-group centers (blue) contributed heavily to peak B. The contribution of the core atoms (orange) existed only at low q, below 0.7 Å^{-1}. Although the position of the core peak did not match up to peak A of the simulated structure factors, it did align more closely with the position of peak A in the experimental WAXS

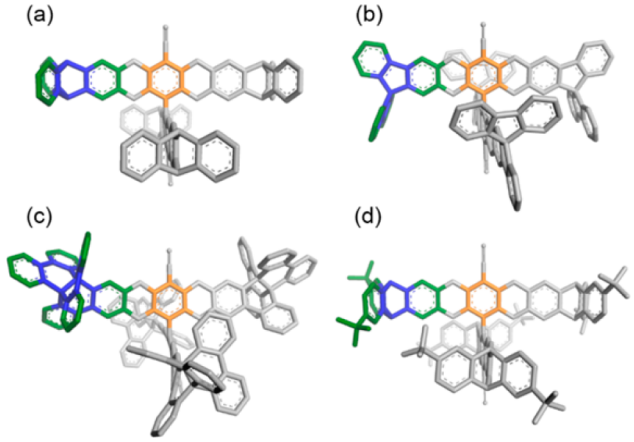

Figure 5. Molecular models of (a) OMIM-1, (b) OMIM-2, (c) OMIM-3, and (d) OMIM-4 showing atom groups of interest. The core atoms are shown in orange, the inner end-group atoms in blue, and the outer end-group atoms in green. For clarity, the groups are colored on one arm only, whereas the remaining atoms are left gray. Hydrogen atoms are not shown.

dx.doi.org/10.1021/jp308798u | J. Phys. Chem. B 2013, 117, 355−364

data. It should be noted that the structure factors showed significant variability among independent simulation boxes in this low-q region (as illustrated by the error bars given in Figure S4 of the Supporting Information), which may account for the shift of peak A in the simulated structure factors compared to the WAXS data. The position ranges for peaks A, B, and C for OMIMs 1−4 are summarized in Table 3 along with the interpretations provided by the partial structure factors from the simulations.

Table 3. Experimental Scattering Peak Positions and Interpretations[a]

peak	q (Å^{-1})	d (Å)	interpretation
A	0.31−0.376	16.7−20.5	separation between nearest-neighbor molecules
B	0.76−0.95	6.6−8.3	separation between inner end-group atoms (end-group centers)
C	1.22−1.43	4.4−5.1	separation between outer end-group atoms

[a]Peak positions are given here as a range for all biphenyl-core OMIMs. Specific positions for each individual OMIM are given in Table S4 of the Supporting Information.

The slight association of peak A with the core atoms suggests that this peak is likely related to the distance between nearest-neighbor molecules. With bulkier end groups, the molecules occupy a larger volume, which results in an increase in the separation distance between neighboring molecules (16.7 to 20.5 Å). Correspondingly, a shift in peak A to lower q was observed with increasing end-group bulkiness and OMIM size. From the partial structure factors, peak B was attributed to the inner end-group atoms or end-group centers. As was observed for peak A, the increased bulkiness of the end-groups caused a larger separation between neighboring end-group centers (6.6−8.3 Å), resulting similarly in a shift of peak B to lower q. Note that no strong peak B was present in the OMIM-4 scattering pattern (Figure 4d). This is due to the fact that the bulk of the end groups is not located at the center but at the outer *tert*-butyl atoms. Lastly, peak C was observed to be related to the separation distance between outer end-group atoms. The position of this peak is similar for OMIMs 1−3 (~4.5 Å), but is shifted to larger separation distances for OMIM-4 (5.1 Å). This suggests that the bulky *tert*-butyl groups of OMIM-4 effectively forced further separation between end groups, corresponding to the shift of peak C to lower q. The resulting less efficient packing of OMIM-4 is consistent with the larger porosity observed for it over the other OMIMs.

3.4. Shape-Persistence of Biphenyl-Core OMIMs. In the design of OMIMs, it was expected that bulky end groups would allow for the formation of internal cavities near the cores, since these end groups would prevent interpenetration of neighboring molecules. Upon visual inspection of the simulations, however, a surprising degree of flexibility was observed. Much of the structural distortion originated at three "weak points" identified within the molecules: (a) bending at the dioxin ring, (b) bending or folding about the single carbon−carbon bond of the biphenyl-core, and (c) rotation about the single carbon−carbon bond of the biphenyl-core in a scissor-like fashion. Angle distributions measuring these three weak points for all of the biphenyl-core OMIMs are given in Figure S5 of the Supporting Information, along with structures identifying the atoms composing the angle measurements. In comparison to aromatic rings within the structures, the dioxin rings showed a much broader distribution of angle bending. Similarly, the broad distributions of bending and rotation about the biphenyl-core were indicative of a large degree of flexibility within the molecular structures.

The flexibility achieved by the molecules enabled them to bend and twist in attempt to increase attractive intra- and intermolecular interactions, which resulted in essentially a collapse of the molecular structure to provide a more efficient packing and hence decreased porosity. Cooperative structural distortion of the molecules through weak points such as those discussed above resulted in open and closed molecular structures. Open structures (see example in Figure S6a of the Supporting Information) can be considered those that are most shape-persistent, such that the original X-shape of the molecule is maintained through roughly 90° angles at the biphenyl core. However, through cooperative bending and twisting, importantly scissor-like rotation about the core, closed structures (see example in Figure S6b of the Supporting Information) are achieved where the shape-persistence and molecular concavities are lost. These closed molecular configurations likely allow for a more efficient packing of the molecules and result in lower porosity throughout the system. It is important to note that flexibility of the OMIMs does not have to occur in a symmetric fashion but may take on many forms (see examples in Figure S6c of the Supporting Information).

To provide a quantitative measure of the cooperative structural distortion arising in the molecules, intramolecular separation distances between end groups were measured. Separation distances were considered only between end groups on opposite halves of the molecules (indicated by the arrows in Figure S6 of the Supporting Information) to provide an indirect measure of the scissor-like rotation about the core. A system of ideal open configurations (Figure S6a of the Supporting Information), with core angles of about 90°, would have a sharp distribution of intramolecular end-group separation distances centered about an equilibrium distance. For comparison across systems, the distributions are reported here as the percent deviation of the separation distance, d, from the equilibrium distance, d_0, i.e., $(d - d_0)/d_0 \times 100$.

In Figure 6a, distributions are shown for the OMIM-1 simulations at different densities. Three peaks are observed near −30, −5, and 15%. The central peak at −5% arises from open configurations, where all of the intramolecular end-group separation distances are nearly at the equilibrium value. A slight deviation of this peak from 0% is likely the result of the numerous intra- and intermolecular interactions in the packed state. The outer peaks at −30 and 15%, on the other hand, can be attributed to closed structures. Comparison of these peaks provides an estimation of the proportion of open and closed configurations in the packed systems. As the density of the OMIM-1 system is increased, the intensity of the peak at −5% decreases, suggesting that many open configurations have rearranged into closed structures. This is not surprising since the higher density packing arrangements would feel higher stress due to increased interactions, which would drive greater distortion of the molecular structures. At the highest packing density, the peaks at −5 and 15% have essentially merged into one large peak, whereas the peak at −30% remains relatively unchanged. This peak at −30% corresponds to short intramolecular end-groups separation distances, where end-groups are held next to each other by strong attractive intramolecular interactions between the end-group atoms. Conversely, the larger intramolecular end-group separation

dx.doi.org/10.1021/jp308798u | J. Phys. Chem. B 2013, 117, 355−364

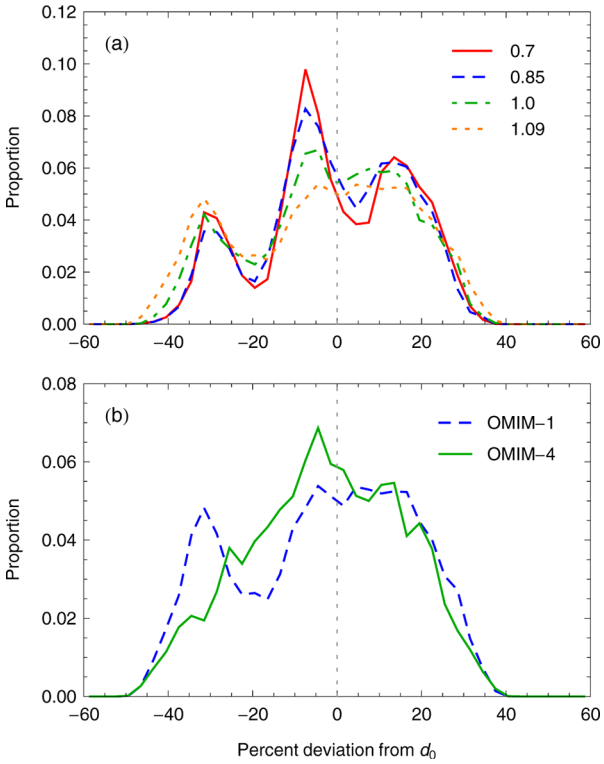

Figure 6. Distributions of the percent deviation of intramolecular end-group separation distances from an equilibrium value, d_0, which provide an indication of the proportion of open and closed structures of OMIMs through an indirect measure of the scissor-like motion of the molecules. A comparison of the distributions is provided for (a) OMIM-1 at various densities (0.7, 0.85, 1.0, and 1.09 g cm^{-3}) and (b) OMIM-1 and OMIM-4 using method 4.

distances that contribute to the peaks at −5 and 15% are also heavily influenced by intermolecular interactions of neighboring molecules.

The distributions of intramolecular end-group separation distances for all biphenyl-core OMIMs yielded useful insight into the impact of the end groups on packing behavior. Figure 6b shows a comparison of these distributions for OMIMs 1 and 4, while the distributions of all biphenyl-core OMIMs are given in Figure S7 of the Supporting Information. The comparison of OMIMs 1 and 4 is particularly interesting since OMIM-4 shares the same end group as OMIM-1 with only the addition of *tert*-butyl groups. Unlike the distribution for OMIM-1, OMIM-4 has a broad distribution with a single main peak centered nearly at the equilibrium distance, around −5%, and no strong peak at close separation distances near −30%, like was observed in OMIM-1. Thus, the bulky *tert*-butyl groups more affectively held apart the end groups to maintain a larger proportion of open structures. This finding is consistent with the greater porosity observed for OMIM-4 in comparison to OMIM-1, which had a larger proportion of closed structures. OMIM-2 produced a distribution similar to OMIM-1 with distinct peaks at small and large separation distances, indicative of a large proportion of closed structures. OMIM-3 showed a narrower distribution than OMIMs 1 and 2, centralized around −20%. The bulky end groups of OMIM-3 provided strong attractive interactions, causing some deviation from the equilibrium distance, but the bulkiness of the end group also helped to push apart the end groups farther than was observed for OMIMs 1 and 2, which showed the nearest peak at −30%. Thus, the intramolecular end-group separation distributions suggest that OMIMs 1 and 2 are more flexible, while OMIMs 3 and 4 are more rigid and shape-persistent. This is consistent with the porosities measured, as OMIMs 3 and 4 had the highest surface areas and pore volumes.

The distributions in Figure 6 and Figure S7 only consider intramolecular distances within the systems. However, the intermolecular interactions of end groups are also important, as interpenetration of neighboring molecules will lead to decreased porosity. Therefore, radial distribution functions (RDFs) were calculated for the centers of all the end-group atoms within the system. The RDFs of the end-group centers of OMIMs 1 and 3 are given in Figure 7 and those for all

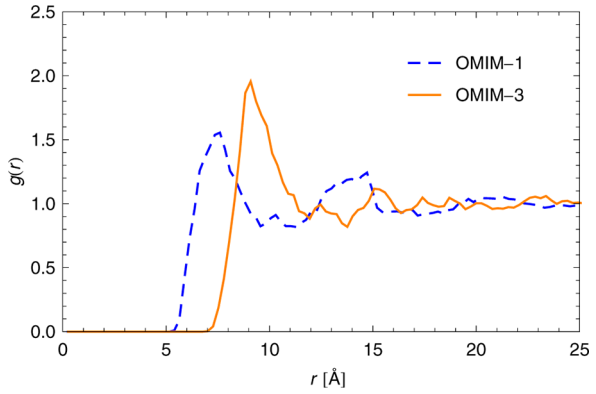

Figure 7. Radial distribution functions, $g(r)$, of end-group centers for OMIM-1 and OMIM-3. The end group centers are taken as the geometric center of the atoms colored blue in Figure 5. The radial distribution functions of all biphenyl-core OMIMs are given in Figure S8 of the Supporting Information.

biphenyl-core OMIMs are provided in Figure S8 of the Supporting Information. The peaks in the RDFs show a shift to larger separation distances from OMIM-1 (∼7 Å) to OMIM-3 (∼9 Å), suggesting that the bulkier end groups of OMIM-3 create a less efficient packing. Interestingly, the RDF of OMIM-4 (Figure S8) has no strong peak. This is likely because the bulk of its end groups remain at the outer edges with the *tert*-butyl groups and not at the center. For all biphenyl-core OMIMs, small peaks were observed near 15 Å, which can be attributed to intramolecular distances between end-groups on the same molecule. It is important to note that the position of the RDF peaks are consistent with scattering peak B observed to be associated with inner end-group atoms (Figure 4 and Table 3). The lack of a peak for OMIM-4 is also consistent with the disappearance of peak B in the scattering of OMIM-4 (Figure 4d).

By understanding the structures of the molecules and the impact of their weak points on the packing behavior, important design principles can be identified to increase the porosity of the OMIMs. First, the shape-persistence of OMIMs 3 and 4 provided greater porosity. In these cases, the bulky end groups of OMIM-3 and bulky *tert*-butyl groups of OMIM-4 hindered the free rotation about the core such that the molecular concavities were better maintained. The greater flexibility of OMIMs 1 and 2, on the other hand, caused a collapse of the molecular structures and reduced porosity. The second observation is that, while bulky end groups help to provide shape-persistence, they can also have a pore filling effect. This is illustrated most clearly by comparison of OMIMs 3 and 4.

dx.doi.org/10.1021/jp308798u | J. Phys. Chem. B 2013, 117, 355−364

Although both showed little rotation about the core, OMIM-4 achieved a greater surface area and pore volume. The much bulkier end groups of OMIM-3 likely filled some of the pore space. Analogous is the comparison of OMIMs 1 and 2. While both were able to rotate freely about the core, OMIM-1 achieved higher porosity since the bulkier end groups of OMIM-2 had a similar pore-filling effect. Therefore, in the design of OMIMs, it is important to have shape-persistent concavities aided by bulky end groups that hinder collapse of the molecular concavities, but it is equally important that the end groups are not so bulky that they fill potential pore space.

3.5. Reexamination of Simulation Methods. Given the offered interpretations of the scattering patterns and molecular flexibilities, a better explanation of the dissimilarities in the structure factors of the initial OMIM-1 simulations obtained with different simulation methods (Figure 3) can be provided. For example, differences were observed between the methods in the positions of peak B, which is suggested to be associated with the separation of end-group centers. With methods 1 and 3, peak B was shifted to lower q (or larger distances), while methods 2 and 4 agreed more closely to the true position of peak B in the experimental WAXS data. The closer separation of end groups in methods 2 and 4 suggest a more efficient packing, and likely interpenetration of neighboring molecules, which resulted in lower porosity.

Another important discrepancy between the methods was observed for peak C associated with the separation between outer end-group atoms. This peak was not captured at all by method 1, which consisted of rigid molecules equilibrated by an MC simulated annealing, suggesting that neighboring end groups did not pack closely together. This makes sense, since the rigid molecules were not able to reorganize in order to increase inter- and intramolecular interactions to allow a denser packing; hence, larger porosity was measured in this model. Peak C was captured by methods 2−4, but the position and breadth varied. A narrower peak was observed for methods 2 and 4, which may suggest a stronger interaction between the end groups in that model. This may be due to the inclusion of electrostatic charges in methods 2 and 4 but not in method 3.

The intramolecular contribution to the structure factors were calculated by considering each single molecule within the model independently. The single-molecule and total structure factors for methods 1−4 are given in Figure S9 of the Supporting Information. With all four methods, the single-molecule (intramolecular) contribution to the structure factors had no discernible peak C, suggesting that this peak arises mainly due to interactions between neighboring molecules, such as close packing of the end groups of one molecule into the concavities of nearby molecules. These results reiterate the findings from the comparison of the biphenyl-core OMIMs, which suggested that end groups must be bulky enough to maintain the concavities and internal free volume while preventing interpenetration of neighboring molecules.

4. CONCLUSIONS

Four simulation methods for modeling OMIMs were examined. The first three approaches were fixed-density models utilizing MC and MD techniques. Good agreement was observed with method 2 when a correct system density was specified, but accurate experimental measures are still elusive. In order to allow for predictive simulations with no required input parameters, such as density, method 4 was introduced. This technique utilized a 21-step MD compression protocol that resulted in consistent and realistic system densities that were not fixed. This density-independent method was applied to the set of biphenyl-core OMIMs and validated by comparison to experimental X-ray scattering data, which showed excellent agreement in the peak positions and relative intensities.

Additionally, the molecular models offered necessary atomistic detail to aid in the interpretation of the scattering features. Characteristic distances within the systems associated with the scattering peaks were identified utilizing partial structure factors, which specified peaks associated with the separation distances between nearest-neighbor molecules, end-group centers, and outer end-group atoms. Further analysis of the OMIM simulations provided important insight into the structures of the molecules through understanding of their flexibility and shape-persistence. Bulky and awkward end groups (OMIMs 3 and 4) were found to help maintain the concavities of the molecules for effective pore formation while preventing significant interpenetration of neighboring molecules. The conclusions drawn from these simulations will contribute to the future design of OMIMs by suggesting ways in which the packing behavior of these complex molecules can be hindered further to provide increased porosity. Most importantly, rigidity and shape-persistence of the molecular concavities are required to maintain the intrinsic molecular free volume and aid in micropore formation.

■ ASSOCIATED CONTENT

Supporting Information

Complete details of simulation methods; molecular dynamics equilibration protocols; SAXS data and subtraction of particulate power-law scattering; average atomic displacements during MC simulated annealing of method 1; images of OMIM-2 regioisomers; experimental WAXS peak positions; simulated structure factors with error bars for OMIMs 1−4; angle distributions for ring bending, core bending, and core rotation; example molecule snapshots of open and closed OMIM-1 structures; distributions of the percent deviation of intramolecular end-group separation distances for OMIMs 1−4; radial distribution functions of end-group centers for OMIMs 1−4; single-molecule (intramolecular) structure factors of OMIM-1 using methods 1−4 (PDF). This material is available free of charge via the Internet at http://pubs.acs.org.

■ AUTHOR INFORMATION

Corresponding Author

*E-mail: colina@matse.psu.edu.

Notes

The authors declare no competing financial interest.

■ ACKNOWLEDGMENTS

The authors acknowledge the National Science Foundation (DMR-0908781) and EPSRC (EP/G065144 and EP/H024034) for funding. Computational resources for this research were provided in part by the Materials Simulation Center of the Materials Research Institute, the Research Computing and Cyberinfrastructure unit of Penn State Information Technology Services, and the Penn State Center for Nanoscale Science. AGM was supported by a National Science Foundation Graduate Research Fellowship (DGE-0750756).

REFERENCES

(1) Davis, M. E.; Lobo, R. F. *Chem. Mater.* **1992**, *4*, 756−768.
(2) Eddaoudi, M.; Moler, D. B.; Li, H.; Chen, B.; Reineke, T. M.; O'Keeffe, M.; Yaghi, O. M. *Acc. Chem. Res.* **2001**, *34*, 319−330.
(3) Kitagawa, S.; Kitaura, R.; Noro, S.-i. *Angew. Chem., Int. Ed.* **2004**, *43*, 2334−2375.
(4) Boehm, H. P. *Carbon* **1994**, *32*, 759−769.
(5) Tsyurupa, M. P.; Davankov, V. A. *React. Funct. Polym.* **2006**, *66*, 768−779.
(6) McKeown, N. B.; Budd, P. M. *Macromolecules* **2010**, *43*, 5163−5176.
(7) Mastalerz, M.; Oppel, I. M. *Angew. Chem., Int. Ed.* **2012**, *51*, 5252−5255.
(8) Schneider, M. W.; Oppel, I. M.; Ott, H.; Lechner, L. G.; Hauswald, H.-J. S.; Stoll, R.; Mastalerz, M. *Chem.—Eur. J.* **2012**, *18*, 836−847.
(9) Mastalerz, M.; Schneider, M. W.; Oppel, I. M.; Presly, O. *Angew. Chem., Int. Ed.* **2011**, *50*, 1046−1051.
(10) Bojdys, M. J.; Briggs, M. E.; Jones, J. T. A.; Adams, D. J.; Chong, S. Y.; Schmidtmann, M.; Cooper, A. I. *J. Am. Chem. Soc.* **2011**, *133*, 16566−16571.
(11) Jiang, S.; Jones, J. T. A.; Hasell, T.; Blythe, C. E.; Adams, D. J.; Trewin, A.; Cooper, A. I. *Nat. Commun.* **2011**, *2*, 207.
(12) Chong, J. H.; MacLachlan, M. J. *J. Org. Chem.* **2007**, *72*, 8683−8690.
(13) Chong, J. H.; Ardakani, S. J.; Smith, K. J.; MacLachlan, M. J. *Chem.—Eur. J.* **2009**, *15*, 11824−11828.
(14) Chong, J. H.; MacLachlan, M. J. *Chem. Soc. Rev.* **2009**, *38*, 3301−3315.
(15) Bezzu, C. G.; Abbott, L. J.; Msayib, K. J.; Taylor, R. G. D.; Walker, J.; Colina, C. M.; McDermott, A. G.; Runt, J.; Maynard-Atem, L.; Budd, P. M.; McKeown, N. B. In preparation.
(16) Jiao, Y.; Stillinger, F.; Torquato, S. *Phys. Rev. Lett.* **2008**, *100*, 245504.
(17) Jiao, Y.; Stillinger, F.; Torquato, S. *Phys. Rev. E* **2009**, *79*, 041309.
(18) Rai, N.; Siepmann, J. I. *J. Phys. Chem. B* **2007**, *111*, 10790-10799. See the TraPPE website for additional references and parameters: http://siepmann6.chem.umn.edu/trappe.
(19) Larsen, G. S.; Lin, P.; Hart, K. E.; Colina, C. M. *Macromolecules* **2011**, *44*, 6944−6951.
(20) Plimpton, S. *J. Comput. Phys.* **1995**, *117*, 1-19. See also the LAMMPS website: http://lammps.sandia.gov.
(21) Sun, H. *J. Comput. Chem.* **1994**, *15*, 752−768.
(22) Accelrys Software Inc., *Materials Studio*, Release 5.5, Accelrys Software Inc.: San Diego, 2007.
(23) Jorgensen, W. L.; Maxwell, D. S.; Tirado-Rives, J. *J. Am. Chem. Soc.* **1996**, *118*, 11225−11236.
(24) Hess, B.; Kutzner, C.; van der Spoel, D.; Lindahl, E. *J. Chem. Theory Comput.* **2008**, *4*, 435-447. See also the Gromacs website: http://www.gromacs.org.
(25) Abbott, L. J.; Colina, C. M. *Macromolecules* **2011**, *44*, 4511−4519.
(26) Duren, T.; Millange, F.; Ferey, G.; Walton, K. S.; Snurr, R. Q. *J. Phys. Chem. C* **2007**, *111*, 15350-15356. See also the Duren group website: http://www.see.ed.ac.uk/~tduren/research/surface_area.
(27) Le Roux, S.; Petkov, V. *J. Appl. Crystallogr.* **2010**, *43*, 181-185. See also the ISAACS website: http://www.isaacs.sourceforge.net.
(28) McDermott, A. G.; Larsen, G. S.; Budd, P. M.; Colina, C. M.; Runt, J. *Macromolecules* **2011**, *44*, 14−16.
(29) Budd, P. M.; McKeown, N. B.; Ghanem, B. S.; Msayib, K. J.; Fritsch, D.; Starannikova, L.; Belov, N.; Sanfirova, O.; Yampolskii, Y.; Shantarovich, V. *J. Membr. Sci.* **2008**, *325*, 851−860.